Three-dimensional Numerical Simulations of Rayleigh-Taylor Unstable Flames in Type Ia Supernovae

M. Zingale[1], S. E. Woosley[1], C. A. Rendleman[2], M. S. Day[2], J. B. Bell[2]

ABSTRACT

Flame instabilities play a dominant role in accelerating the burning front to a large fraction of the speed of sound in a Type Ia supernova. We present a three-dimensional numerical simulation of a Rayleigh-Taylor unstable carbon flame, following its evolution through the transition to turbulence. A low Mach number hydrodynamics method is used, freeing us from the harsh timestep restrictions imposed by sound waves. We fully resolve the thermal structure of the flame and its reaction zone, eliminating the need for a flame model. A single density is considered, 1.5×10^7 g cm^{-3}, and half carbon/half oxygen fuel—conditions under which the flame propagated in the flamelet regime in our related two-dimensional study. We compare to a corresponding two-dimensional simulation, and show that while fire-polishing keeps the small features suppressed in two dimensions, turbulence wrinkles the flame on far smaller scales in the three-dimensional case, suggesting that the transition to the distributed burning regime occurs at higher densities in three dimensions. Detailed turbulence diagnostics are provided. We show that the turbulence follows a Kolmogorov spectrum and is highly anisotropic on the large scales, with a much larger integral scale in the direction of gravity. Furthermore, we demonstrate that it becomes more isotropic as it cascades down to small scales. Based on the turbulent statistics and the flame properties of our simulation, we compute the Gibson scale. We show the progress of the turbulent flame through a classic combustion regime diagram, indicating that the flame just enters the distributed burning regime near the end of our simulation.

Subject headings: supernovae: general — white dwarfs — hydrodynamics — nuclear reactions, nucleosynthesis, abundances — conduction — methods: numerical

---

[1]Dept. of Astronomy & Astrophysics, The University of California, Santa Cruz, Santa Cruz, CA 95064

[2]Center for Computational Science and Engineering, Lawrence Berkeley National Laboratory, Berkeley, CA 94720

1. INTRODUCTION

The importance of the Rayleigh-Taylor (RT) instability and turbulence in accelerating a thermonuclear flame in Type Ia supernovae (SNe Ia) is well recognized (Müller & Arnett 1982; Livne 1993; Khokhlov 1995; Niemeyer & Hillebrandt 1995; Gamezo et al. 2003; Reinecke et al. 2002). Nevertheless, the physics of reactive flame instabilities in SNe Ia is still not completely understood. In a previous study (Bell et al. 2004c), we showed the transition of the burning front from the flamelet regime to the distributed burning regime occurred at a density of $\sim 10^7$ g cm^{-3}, through two-dimensional direct numerical simulations. This transition had long been postulated, but these simulations were the first to demonstrate it. It was recently shown that large scale models may incorporate a specialized prescription for distributed burning within the flame model to release more energy, produce higher-velocity ejecta (Röpke & Hillebrandt 2005), and bring them more in line with observations. But the arbitrary nature of these prescriptions underscores the importance of a firm understanding of the distributed burning regime. In the present paper, we extend our study to three dimensions while continuing to fully resolve the thermal structure of the flame. Due to the computational expense of three-dimensional simulations, we concentrate on a single density, 1.5×10^7 g cm^{-3}. In our two-dimensional study, this was in the flamelet regime. In three dimensions, turbulence is expected to play a bigger role (Khokhlov 1994), and wrinkling on even smaller scales could make the transition density to the distributed regime higher in three dimensions than it is in two dimensions. We note that the transition to distributed burning occurs when portions of the flame smaller than the flame thickness become wrinkled. This can occur either through turbulence or the RT instability directly, as demonstrated in our two-dimensional study.

Avoiding the use of a flame model, such as front-tracking (Röpke et al. 2003) or thickened flames (Khokhlov 1993, 1994), allows us to understand the small scale physics of the flame with no prior assumptions. There is no need to set a flame speed—the input physics yield the proper speed automatically, with proper coupling between the flame and the flow. Nor is any subgrid flame model required. In the flamelet regime, the burning sets the smallest physical scale. The importance of curvature in modifying the local burning rate (Dursi et al. 2003) is implicitly accounted for. When turbulence becomes important, scales down to the Gibson scale—the scale at which a turbulent eddy burns away before turning over—need to be followed for a resolved calculation, otherwise, some sort of turbulence subgrid model is likely required. Resolving the thermal structure does constrain the size of the region we can consider to ~ 100 flame thicknesses, due to computational resources. Furthermore, to see RT growth, our domain must be several times wider than the small scale cutoff for

reactive RT, namely, the fire-polishing length,

$$\lambda_{\rm fp} = 4\pi \frac{{S_l}^2}{g_{\rm eff}} \ , \tag{1}$$

(Timmes & Woosley 1992) where $g_{\rm eff}$ is the effective gravitational acceleration and S_l is the laminar flame speed. Since the fire-polishing length grows and the flame thickness decreases with increasing density, these constraints make the region centered around 10^7 g cm^{-3} the optimal density for direct numerical simulations. This is illustrated in Figure 1, where we plot the flame thickness and the fire-polishing lengths as a function of density. We see these lines cross just between $\rho = 10^7$ g cm^{-3} and $\rho = 1.5 \times 10^7$ g cm^{-3}. The shaded region indicates a factor of two uncertainty in the fire-polishing length.

Some measurements of the response of the local burning rate to curvature and strain were provided in one-dimensional spherical flame studies (Dursi et al. 2003) and in our previous study of the Landau-Darrieus instability (Bell et al. 2004b). Here we can assess the difference in the effect of curvature between two and three dimensions, where the surface to volume ratio of the RT unstable flame changes significantly. These small-scale flame studies provide important information on flame physics in SNe Ia that can be used to build a subgrid model for large scale flame simulations where it is no longer possible to resolve the flame structure.

Modeling the flame in three dimensions will also allow us to gain an understanding of the nature of the turbulence. The Kelvin-Helmholtz instabilities accompanying the RT instability in SNe Ia drives most of the turbulence in the star, and, as the flame wrinkles, it will interact with the turbulence generated on larger scales. Three-dimensional simulations of the flame can give us an idea about the nature of this flame-generated turbulence. Specifically, is it isotropic? Does it obey Kolmogorov or Bolgiano-Obukhov statistics (Niemeyer & Kerstein 1997; Chertkov 2003)? Turbulent subgrid models are the foundation of some large scale SNe Ia simulations (Reinecke et al. 2002), but these models always assume the turbulence to be isotropic. Any anisotropy can have a large effect on the progression of the flame front. If the flame burns faster radially than laterally, as initial hot spots rise, these burning spots may not merge, leaving behind unburned fuel. An important question is over what scales does the turbulence remain anisotropic?

Because of the computational demands of three dimensions, the size of the domain that we can consider is limited, and we use large two-dimensional simulations to complement the results of the three-dimensional calculations. This study will give us an idea of how good an approximation the two-dimensional simulations are. Only a single density is considered here, 1.5×10^7 g cm^{-3}, with half carbon/half oxygen fuel. We also compare our results with the thickened-flame model RT simulations performed by Khokhlov (1995). Finally, these

results can be used to directly validate different flame models—a process that is underway, but beyond the scope of the present paper.

In § 2, we outline the basic formulation of our simulation code and input physics used for the present simulations. Results of the two- and three-dimensional RT simulations are presented in § 3, and we conclude in § 4 with a comparison to previous three-dimensional reactive RT simulations.

2. SIMULATION DETAILS

The numerical method is identical to that described in detail in Bell et al. (2004a), and used in our two-dimensional RT study (Bell et al. 2004c), so we only briefly summarize here. A low Mach number formulation of the inviscid Navier-Stokes equations is solved using an advection/projection/reaction formalism. In this approximation, the pressure is decomposed into a dynamic and thermodynamic component, the ratio of which is $O(M^2)$. The thermodynamic component is assumed to be spatially uniform, so that only the dynamic component appears in the momentum equation. As a result, acoustic waves are not supported analytically. The advection algorithm is a conservative second-order accurate unsplit Godunov method, which yields better symmetry and resistance to grid imprinting than corresponding directionally split methods. An elliptic constraint on the velocity field, derived by requiring the thermodynamic pressure to be constant along streamlines, is solved in the projection step. The advantage of the low Mach number formulation is that that the timesteps depend solely on the fluid velocity and not the fluid velocity plus sound speed. As the flames we consider here are $M \ll 1$, this greatly reduces the number of timesteps required, although due to the projection step each timestep requires more computational resources. The reaction step uses a single rate for the $^{12}\mathrm{C}(^{12}\mathrm{C},\gamma)^{24}\mathrm{Mg}$ reaction from Caughlan & Fowler (1988). The thermal conductivities are those from Timmes (2000), and the equation of state is appropriate for electron degenerate matter, as provided in Timmes & Swesty (2000). The code is parallelized using MPI, distributing patches in the mesh hierarchy across processors in a load-balanced fashion (Rendleman et al. 2000). The adaptive mesh refinement (AMR) follows the strategy outlined in Berger & Colella (1989).

Only a single density is considered here, 1.5×10^7 g cm^{-3}, with the fuel half carbon and half oxygen, which, in our two-dimensional study, was comfortably in the flamelet regime. As in the two-dimensional study, only the carbon is burned. The laminar flame speed, S_l, is 8.19×10^3 cm s^{-1} and the thermal flame thickness, δ, is 0.55 to 1.25 cm depending on the

definition. The former corresponds to

$$\delta = \frac{T_{\rm ash} - T_{\rm fuel}}{\max\{|\nabla T|\}} \ , \tag{2}$$

common in terrestrial combustion, while the later is

$$\delta = x(T = 0.9\max\{T\}) - x(T = 0.1\max\{T\}) \ , \tag{3}$$

as used in (Timmes & Woosley 1992). This factor of two uncertainty makes some definitions of the burning regime the flame is operating in uncertain. Unless otherwise indicated, we will use the former definition. The Atwood number of this flame is 0.28.

The base grid for this simulation is $32 \times 32 \times 64$, and covers the entire domain. Four additional levels of adaptive mesh refinement are used, and track the location of the flame surface. Each successive level is a factor of 2 finer, yielding an effective fine grid of $512 \times 512 \times 1024$ zones. We note that this grid is quite large even for non-reactive RT simulations. A recent study comparing several codes simulating the pure RT instability (Dimonte et al. 2004) used grids no larger than $256 \times 256 \times 512$, and found this to be more than adequate to observe the full nonlinear phase of the RT instability development. As we will show in § 3, with this size grid we capture the turbulent cascade over more than one and a half orders of magnitude. The domain is 53.5 cm $\times$ 53.5 cm $\times$ 107.0 cm—the same size as the corresponding two-dimensional simulation from Bell et al. (2004c), yielding a grid resolution of 0.1 cm. This puts just over 5 zones in the flame thickness, which in two-dimensional studies was enough to yield convergence of the flame speed, length, and width (Bell et al. 2004c).

Although momentum transport in a white dwarf is dominated by convective processes so that we may safely neglect physical viscosity terms, burning sets a lower bound on the scale length of the turbulence. The associated length, the Gibson scale, should be resolved on the grid. It is difficult to predict the Gibson scale length, since it depends on the nature of the turbulence, but estimates suggest it to be around 1.0 cm (Niemeyer & Woosley 1997). Based on this estimate, the smallest turbulent eddies that can affect our flame are resolved on our grid. The fire-polishing wavelength is 3.0 cm, so we more than resolve the smallest scale that RT will grow on.

To initialize the problem, a steady-state laminar flame at this density is mapped onto the domain, and shifted about its zero point by a perturbation,

$$\Delta = A \sum_{m=1}^{M} \sum_{n=1}^{N} \delta_{m,n} \ , \tag{4}$$

where

$$\delta_{m,n} = a_{m,n} \sin\left(\frac{2\pi m x}{L_x} + \phi^x_{m,n}\right) \sin\left(\frac{2\pi n y}{L_y} + \phi^y_{m,n}\right) \ , \tag{5}$$

with $\phi^x_{m,n}$ and $\phi^y_{m,n}$ chosen randomly, and $a_{m,n}$ chosen randomly to fall between -1 and 1. Here, L_x and L_y are the size of the domain in the x- and y-direction respectively. The overall amplitude, A is set to make the maximum perturbation $\Delta = 1$ cm. For the present simulation, we pick $M = N = 10$. At the lower boundary ($-$Z), fuel enters the domain at the laminar flame speed. The upper boundary (+Z) is outflow, and the transverse directions are periodic. Because of the inflow conditions, an unperturbed flame would remain stationary in our domain. Gravity points in the z-direction, and is taken as 10^9 cm s^{-2}.

The run begins relatively unrefined, with the fine grid taking up less than 10% of the domain, but as the non-linear RT develops, the number of zones grows to over 160 million, with the fine grid covering almost half of the domain. In all, 395 coarse grid timesteps were taken, corresponding to approximately 1.2 ms of physical evolution. The simulation was stopped when the RT spikes began to approach the upper boundary. The 2:1 aspect ratio of our domain means that this will occur when the mixed region becomes larger than the width of the domain, after this point there are no more modes that can grow in the periodic domain. For comparison, the identical setup is run in two dimensions.

3. RESULTS

Figure 2 shows a volume rendering of the carbon mass fraction at several instances in time. Throughout this section, we will refer to them by the letter key for each panel. As the simulation begins, the initial perturbations burn away prior to the linear-growth phase of the RT instability. The seeded modes grow strongly, creating a highly wrinkled flame surface. The initial growth of the RT instability and the smooth fire-polished features between the characteristic RT mushroom caps looks very similar to the early two-dimensional evolution, as shown in Figure 3. These growing bubbles begin to interact and merge, creating a more extended mixed region. In Figures 2c,d, these modes begin to break down as they become wrinkled on increasingly smaller scales. This provides a first indication that turbulence is operating on scales smaller than the fire-polishing length. At late times, Figure 2e,f, we see a very chaotic flame. It has become quite thick and it is hard to discern the original modes we seeded, as they have broken down into a more turbulent flame. This stage of the flame evolution has no two-dimensional analogue.

Figures 4–6 show the flame speed, relative change in surface area, and width of the mixed region for the two- and three-dimensional runs. The effective flame speed is computed by looking at the carbon consumption rate on the domain, as detailed in Bell et al. (2004c). The flame surface area is computed by evaluating the area (length in two dimensions) for instantaneous isosurfaces of constant carbon mass fraction. The carbon mass fraction may

be averaged laterally across the domain to define a mean progress variable as a function of z only. The width of the mixed region is then defined as the distance separating the resulting 0.05 and 0.45 elevations of the mean progress.

We see a similar trend in the effective flame speed (Figure 4) in two and three dimensions in the early stages of evolution. The curve for three dimensions is smoother, since there are more modes growing (due to the extra dimension) and therefore the effect of a single spike of fuel burning away is lessened. Both curves show an initial decline in the flame speed, as the initial perturbations start to burn away before the RT growth sets in. After about 0.0005 s, the RT begins to set in strongly, and the flame speed accelerates to about twice the laminar value. However, at late times, we see the effects of the turbulence in three dimensions, and the flame speed accelerates again. In the two-dimensional case, the flame speed saturates after about 0.7 ms. The saturation is likely due to the finite-size domain, and a higher peak value would be observed in a larger domain.

Figure 5 shows the surface area evolution for the two runs. For each case, two curves are shown, using carbon mass fraction values of 0.25 and 0.1. To allow for a comparison between the two- and three-dimensional runs, we plot the fractional difference of the area,

$$f = \frac{A(t) - A_0}{A_0} \ , \tag{6}$$

where A_0 is the cross-sectional area of the domain. For both dimensions, we see a delay in the growth of the flame surface area as the burning eats away at the initial perturbations. Nevertheless, the linear growth of the RT instability quickly sets in, and we see the flame surface area grow faster in the three-dimensional case than the corresponding two-dimensional simulation after 0.0004 s. The surface area is somewhat sensitive to the value of the carbon mass fraction being used, differing by about 25% at late times in the three-dimensional case. Isosurfaces of the two mass fraction values at a representative time of $t = 0.1$ ms are shown in Figure 7. The 0.25-surface exhibits a higher level of fine-scale structure, resulting in a larger surface area. However, both surfaces exhibit similar trends. By the end of the simulation, the three-dimensional case shows a factor of 12-15 enhancement in flame area.

The width of the mixed region shows the effect of this greater surface to volume ratio in three dimensions clearly. Each simulation has two curves, the interface of the fuel and the mixed region (the top curve for each simulation) and the interface of the ash and the mixed region. The fuel/mixed interface appears choppy, because this is where the spikes of fuel are falling into the hot ash and rapidly burning away. In three dimensions, these spikes of fuel burn away much more rapidly, and, as Figure 6 shows, this interface grows much slower in three dimensions than two dimensions. This is to be contrasted with non-reactive RT simulations (see for example Young et al. 2001; Calder et al. 2002; Dimonte et al. 2004)

that show the three-dimensional case growing faster than the two-dimensional case. When reactions are added, the increase in the surface to volume ratio of the spikes of fuel makes the three-dimensional growth slower than the corresponding two-dimensional case. At late times, once turbulence has set in, we see a departure of the bubbles of ash pushing into the cool fuel from the smooth curve characteristic of the RT instability observed in two dimensions.

Figure 8 shows a volume rendering of the magnitude of the carbon destruction rate at a late time, showing that it is strongly peaked in small regions. Slices of carbon destruction rate are shown in Figure 9. There is considerable small-scale structure present, which perturbs the flame and breaks up the reacting region. This can be compared to the two-dimensional calculation, as shown in Figure 10. The limits of the colormap are chosen to match the laminar rate, but values over 10 times the laminar burning rate are present in both RT calculations.

We pointed out in our previous work (Bell et al. 2004c) that in two-dimensions the flame speed increases slower than the flame surface area, due to the effects of curvature and strain. From Figures 4 and 5, we can see how this trend differs with dimensionality. While the flame speeds in two and three dimensions track each other reasonably well, the relative flame area change is larger in the three-dimensional run. This suggests that in three dimensions, for the density and length scales considered, the curvature and strain effects may be much more important in determining the local fuel consumption rate, since the growth in flame area is much more than overall increase in flame speed.

As Figure 2 shows, at late times, energy in the large scales has cascaded to small scales and creates considerable structure in the 3D flame. This effect was is observed in the two-dimensional results, shown in Figure 3. The increased flame surface complexity in three dimensions was also reported in Khokhlov (1994).

The power spectrum of the velocity field can be used to characterize the turbulent fluctuations. However, because our domain is not triply-periodic, there is a preferred direction (the direction of the flame propagation) in which we see a jump in velocity across the flame. We note that the velocity field can be written as the sum of a divergence free term and the gradient of a scalar. We can further decompose the latter component:

$$\mathbf{u} = \mathbf{u}_d + \nabla\phi + \nabla\psi \ . \tag{7}$$

Here $\mathbf{u}_d$ is the divergence free velocity field subject to $\mathbf{u}_d \cdot \mathbf{n} = 0$ on the boundaries, $\nabla\phi$ is the compressible component, while $\nabla\psi$ accommodates the velocity jump due to the inflow and outflow boundary conditions. Only the divergence-free part of the velocity field is considered when computing the power spectrum. We decompose the velocity field using a projection

operation similar to the projection step in the main hydrodynamics algorithm (Bell et al. 2004a). Since the vorticity level is negligible at the boundaries, we can treat $\mathbf{u}_d$ as though it were periodic in z, interpolate it onto a uniform grid at the finest resolution and decompose the resulting field using a standard FFT algorithm. We then define the power spectrum

$$E(K) = \int_{K=|k|} \mathrm{d}k \, (\hat{u}(k)^2 + \hat{v}(k)^2 + \hat{w}(k)^2) \,, \tag{8}$$

where $\hat{u}(k)$, $\hat{v}(k)$, and $\hat{w}(k)$, are the Fourier transforms of the x, y, and z components of the divergence free velocity field. This integral is evaluated by summing the integrand over spherical shells of constant radius $k = \sqrt{k_x^2 + k_x^2 + k_z^2}$ and unit wavenumber thickness.

Figure 2 shows the power spectrum along side the carbon mass fraction rendering for several different times. Two curves are shown in the power spectrum; the solid line represents the spectrum of the projected component, while the dashed line represents that of the unprojected field. At early time, we see substantial discrepancy in the two curves illustrating the imprint of the flame on the spectrum. At later times, this effect dissipates as the energy in the vortical component increases. The spikes at the highest wavenumbers are due to jumps in refinement in the AMR grid. As the RT instability evolves, the high wavenumbers begin to follow a Kolmogorov spectrum, $E(k) \sim k^{-5/3}$, shown as a gray line in the figures. We can compare the power spectra to the corresponding carbon mass fraction volume rendering alongside it in Figure 2. We first achieve the $-5/3$ scaling in panel d, and comparing the associated image to the previous ones, we see that the transition to turbulence is marked by significant wrinkling on the smallest scales. Prior to panel d, the flame surface remains quite smooth on these small scales due to fire-polishing.

In the final panel, the Kolmogorov turbulence spans about a decade and a half in spatial scales. Figure 11 shows the final three power spectra (panels d-f) plotted on the same axes. We see that the small scale cutoff to the turbulent cascade does not move once we are fully turbulent. We also note that the fire-polishing length (3.0 cm) corresponds to a wavenumber, k_{fp}, of 18 (since $\lambda k = L$, the size of our domain), and the flame thickness ($\delta = 0.55$ to 1.25 depending on the definition) corresponds to a wavenumber, k_δ, of 98 to 43. We highlight these in Figure 11. In these late time power spectra, the turbulent cascade follows the Kolmogorov scaling well past the fire-polishing wavelength, proving that the turbulence is affecting the flame on scales that the RT alone cannot. The cutoff occurs around the flame thickness.

Now that we have determined that the spectrum of turbulence follows Kolmogorov-like scaling, we can compute the integral scale and turbulent intensities in each direction and

define a measure of anisotropy. The turbulent integral scale is defined as

$$l_t^{(x)} = \left(\frac{1}{\int_\Omega \mathrm{d}\Omega \, u^2} \right) \int_{\xi=0}^{L_x/2} \mathrm{d}\xi \int_\Omega \mathrm{d}\Omega \; u(x,y,z)\, u(x+\xi,y,z) \;\; , \tag{9}$$

(Peters 2000) and is a measure of how correlated the velocity is in x-direction. Here, u is the x-component of the velocity, L_x is the physical size of the domain the x-direction, and Ω represents the computational domain. We note that because we use periodic boundaries, the ξ integral is only over half of the domain. A similar definition is used for the y and z integral scales. We also define the turbulent intensity,

$$u' = \sqrt{\int_\Omega \mathrm{d}\Omega (u-\bar{u})^2} \, , \tag{10}$$

where $\bar{u}$ is the average x-velocity (Peters 2000). We perform all these integrals on the projected velocity field. Table 1 lists these parameters for the six snapshots shown in Figure 2. The integral properties in x and y match well, but in the vertical direction, z, both the integral scale and the turbulent intensities are much larger; the turbulence is significantly anisotropic. As an alternative approach to quantifying the anisotropy, we plot two-point correlations in each direction as a function length (ie, plot the magnitude of the ξ integral in eq. [9] as a function of separation distance). Figure 12 shows this quantity separately for each coordinate direction based on the data plotted in Figure 2f. The two-point correlations for the x and y-directions track each other well, even showing a strong anti-correlation in the range $8-23$ cm. In the z-direction, we see the curve is much more broad, demonstrating the larger integral scale.

An interesting question to ask is whether the turbulent field remains anisotropic on all length scales. We expect anisotropy on the largest scales, since gravity is the dominant force term, but as the eddies interact and cascade to smaller scales, the flow could become more isotropic. In the computation of the power spectrum, Eq. (8), we integrated over spherical shells of constant radial wavenumber, thus washing out any information on anisotropy. We can look directly at isosurfaces of $E(k_x, k_y, k_z)$ in Fourier space to see how the degree of anisotropy varies with wavenumber, and therefore, physical scale. A simplification we can make is to average over the cylindrical angle in the k_x-k_y plane, since we are isotropic in the direction transverse to gravity. Then we have

$$E(k_r, k_z) = \left(\frac{1}{\int_{k_r=|k'|} \mathrm{d}k} \right) \int_{k_r=|k'|} \mathrm{d}k \; E(k_x, k_y, k_z) \;\; , \tag{11}$$

where $k' = \sqrt{k_x^2 + k_y^2}$. If the turbulent kinetic energy were isotropic, we would expect contours of constant $E(k_r, k_z)$ to be circles in the k_r-k_z plane, and the largest scales in

the flow would correspond to circles of smaller radius. Figure 13 shows these contours for several values of $E(k_r, k_z)$, every decade from 10 to 10^6 cm^2 s^{-2}. In the left panel, we look at the smallest wavenumbers. We see that the innermost curves are not at all circular—demonstrating that at the largest scales, we are quite anisotropic. This supports the findings from the integral scale and turbulent intensity comparison. As we go to higher wavenumbers, the contours become more and more circular, demonstrating that the turbulence becomes more isotropic as it cascades down to smaller scales. The outermost contour matches a radial wavenumber of ~ 60, which is close to the highest wavenumber still within our turbulent cascade. We conclude that once the turbulence has cascaded down through about an order of magnitude of length scales, it is practically isotropic.

We see that our laminar flame speed is much smaller than the turbulent velocities at late times. In previous work that looked at the scaling of the turbulent flame speed with area enhancement, the smallest ratio of laminar speed to turbulent velocity considered was $S_l/w' = 0.95$ (Niemeyer et al. 1999), at which they found reasonable scaling of the turbulent flame speed to the area enhancement. Here, we reach a point where $S_l/w' = 0.3$, and the dominance of the turbulent velocity over the laminar flame speed in our calculation results in a large departure from perfect scaling of the turbulent flame speed to the area enhancement.

A common estimate of the turbulent velocity is to apply the Sharp-Wheeler scaling for non-reactive RT:

$$v_{\mathrm{RT}} \sim \frac{1}{2}\sqrt{\mathrm{At}\, gL} \tag{12}$$

(Sharp 1984; Davies & Taylor 1950), where At is the Atwood number and L is the integral scale of the turbulence. This is the magnitude of the velocity due to RT growth. If we consider the z direction only—since this is the direction where RT is doing the most work, we find $v_{\mathrm{RT}} = 2.7 \times 10^4$ cm s^{-1} for case f, just slightly above the measured w'. This supports the idea that the turbulence cascade is the result of the RT instability. It is unclear what the analog of equation (12) should be for the transverse directions.

In turbulent combustion, the turbulence will affect the flame on all scales down to the one where the flame can burn away an eddy before its turnover time. This scale, the Gibson scale, represents the smallest turbulent scale that can influence the flame, and together with the flame thickness and fire-polishing length are the minimum scales required to resolve on our grid without including explicit subgrid models for turbulence of the flame. The Gibson scale is

$$l_G = l_t \left(\frac{S_l}{u'}\right)^3 \tag{13}$$

(Peters 2000) for Kolmogorov turbulence (although, Khokhlov 1995 argues the true scale is a factor of ~ 500 larger because of flame speed enhancements due to cusping). Again,

due to the anisotropy, this can vary with direction, but the result falls between 0.38 and 0.44 cm using the data from Table 1. We note that this is very close to our flame thickness, 0.55 cm, and about a 4 zone resolution, so it should just be resolved on our grid. Although we note that since we are not using an explicit viscosity in our calculation, we would expect the cascade to cutoff here due to numerical viscosity as well.

Figure 14 shows a combustion diagram (Poinsot & Veynante 2001; Peters 2000), used in terrestrial combustion for determining the flame regime. Three sets of points are provided, using the x, y, and z integral scales and turbulent intensities separately. The vertical axis is the turbulent intensity divided by the laminar flame speed and the horizontal axis is the integral scale divided by the flame thickness. The different combustion regimes are separated by lines of unit Karlovitz number (the ratio of the nuclear reaction timescale to the Kolmogorov time), unit Damköhler number (the ratio of the largest eddy turnover time to the nuclear reaction time scale) and forces at the integral scale) (Poinsot & Veynante 2001). The flame begins in the lower-left region of the diagram and evolves toward the top-right with time. The points corresponding to the z-based integral quantities are always more to the upper right of the corresponding x- and y-based points. The final points appear to cross the line of constant Karlovitz number, suggesting that in three dimensions, we enter the distributed burning regime at this density. This is supported by our measurement of the Gibson scale, being just below the flame thickness. We note that we used equation (2) for the flame thickness, and because of this ambiguity in the definition, these points would shift to the upper-left using equation (3).

4. CONCLUSIONS

We presented a three-dimensional simulation of an RT unstable flame in SNe Ia, following the evolution into the fully turbulent regime—the first such calculations performed without a flame model. We showed that the growth of the mixed region is slightly faster in two dimensions than in three, but at late times, turbulence takes over in the three-dimensional case, providing a large late-time acceleration of fuel consumption. Curvature and strain effects apparently play a larger role in the three-dimensional simulations, since the relative surface area increases much more in the three-dimensional case than in the two-dimensional case (Figure 5), for roughly the same increase in flame speed over the course of the calculation. Any model of burning in SNe Ia should therefore be based on three-dimensional results, in agreement with conclusions presented in Khokhlov (1994).

The turbulence is Kolmogorov in nature as we showed, with the energy spectrum at late times follows a $-5/3$ power law scaling in wavenumber for over one and a half orders

of magnitude. Apparently the previously postulated Bolgiano-Obukhov statistics (Niemeyer & Kerstein 1997) are not relevant to this Type Ia supernova regime, or perhaps apply only to data from two dimensional (Chertkov 2003) models. We also demonstrated that our turbulent cascade reached the smallest scales permitted by the resolution capabilities of our numerical algorithm on this grid. The turbulent intensities are consistent with the velocities expected from the pure RT instability (eq. [12]), suggesting that it is being driven by the large scale RT growth. In a real star, there will be even larger scales that are RT unstable, suggesting that a 'supergrid' model should be applied to force our domain with the expected intensities. This is a separate problem and could be the focus of future simulations.

The turbulence is strongly anisotropic on the largest scales—with the integral length scale in the vertical direction more than five times that in the transverse directions. But as we showed, the turbulence becomes more isotropic at smaller scales. The inertial range of the turbulence in full star calculations is less than two orders of magnitude, since at the largest scale, stellar flows are not turbulent and the computing hardware and computing algorithm sets a minimum resolvable scale. At the very largest scales, gravity drives anisotropic fluctuations. Based on our measurements of the anisotropy, a minimum of a decade of length scales must be properly represented on the grid in order to permit valid use of an isotropic subgrid model. The assumption of isotropy is currently employed in many turbulent subgrid models, notably (Reinecke et al. 2002), and our findings appear to verify this, provided that a sufficiently large interval of the turbulence spectrum is accurately simulated. Isotropic subgrid scale turbulence would predict isotropic turbulent flame speeds and lead to regular, somewhat spherical expansion of any ignition points. The situation would be quite different if anisotropy of the turbulence were important on the small scales. We would then expect the burning in the direction of gravity to greatly out-pace the lateral burning. This may mean that more ignition points would be required in an anisotropic turbulence-based simulation to match the characteristics of an isotropic turbulence-based simulation.

Previously, the differences between two- and three-dimensional RT flames were explored by Khokhlov (1994, 1995). These calculations employed a thick-flame model, where the flame thickness was stretched to be resolvable on the grid. These thickened-flames did not however employ a subgrid model, so they will neglect the interactions between the flame and the turbulence on scales between the real flame thickness and its thickened counterpart. The present calculations resolve the fire-polishing length, the flame thickness, and the Gibson scale.

The transition to distributed burning occurs when wrinkling occurs on scales smaller than the flame thickness. There are two dominant mechanisms for this wrinkling in Type Ia supernovae—turbulence and the RT instability. In our two-dimensional study, only the

RT instability influenced the flame, because of the nature of two-dimensional turbulence, so the transition to distributed burning occurs at the density where the fire-polishing length becomes smaller than the flame thickness. As we see in the present study, the three-dimensional turbulent cascade can reach scales smaller than the fire-polishing length and greatly wrinkle the flame on scales not possible in two dimensions. This wrinkling will occur on scales down to the Gibson length, where the small eddies can then burn away before they can perturb the flame. We presented a combustion diagram, common in studies of terrestrial flames, which suggests that at this density, the simulation evolves into the distributed burning regime.

Khokhlov (1994) concluded that more small scale structure was present in the three-dimensional simulations, due to the nature of the turbulent cascade in three dimensions. We show overwhelming support for this in our simulations, as shown in Figures 2 and 3. Khokhlov (1994) argues that this difference is most important when the turbulence from the nonlinear RT cascades to higher wavenumber (as it only can do in three dimensions) and reaches scales smaller than the fire-polishing length, and that it is this small scale turbulence that further wrinkles the flame thereby increasing the energy generation rate. With a grid that is effectively $512 \times 512 \times 1024$ zones, we expect that we are modeling the turbulence quite well. At late times, we see a $-5/3$ power law for the turbulent spectrum, in agreement with Kolmogorov theory. The two- and three-dimensional integral quantities (flame speed, surface area, and width) track each other well up to the onset of turbulence.

In our simulations, we never reach a point where the flame speed reaches a steady state, as reported in Khokhlov (1995)—nor do we expect to. The only time such an effect was seen was in the narrowest run of our distributed regime flame in our two-dimensional study (Bell et al. 2004c), where we simply run out of modes to grow in our box—the instability saturates. In the real problem, this arrangement will not occur. The burning rate along the surface of the flame varies tremendously due to curvature and strain, reaching up to $12\times$ the laminar value. It is simply not the case, for our simulation, that the overall effective flame speed is the surface area enhancement multiplied by the laminar flame speed.

Our calculations were performed at a density of 1.5×10^7 g cm^{-3}. Because of our requirement to resolve the flame thickness while fitting the fire-polishing length and Gibson scale on the grid (as shown in Figure 1), we are unable to perform simulations at the 10^8 g cm^{-3} density considered previously by Khokhlov (1994, 1995). We found that the Gibson scale is ~ 0.4 cm, very close to the 1.0 cm estimate by Niemeyer & Woosley (1997). Therefore, our flame is in a regime where the fire-polishing length, Gibson scale, and flame thickness are all of the same order of magnitude. The calculations presented by Khokhlov (1994, 1995) at a density of 10^8 g cm^{-3} have a true flame thickness of 2.75×10^{-2} cm (Timmes & Woosley 1992), which is much smaller than estimates of the Gibson scale at

that density (Niemeyer & Woosley 1997) or the fire-polishing length (5×10^4 cm, according to Khokhlov 1994). The thickened flame thickness is several grid cells in his calculation, or $\sim 10^5$ cm, which is much larger than the Gibson scale, and of the same order as the fire-polishing length. Since the flame-thickening used in these calculations does not account for the turbulence interactions on scales between the true flame thickness and the Gibson scale (such as through an efficiency function as in Colin et al. 2000), it is likely that much of the actual burning is neglected. The optimization of an efficiency function approach for correcting thick-flame RT calculations will be the subject of a future study.

There are also differences in the range of length scales captured in the simulations. The grid employed in Khokhlov (1995) ranged from 32 to 85 zones across and 256 to 512 in the vertical direction. The inertial range representable on this grid is quite small; it is unlikely that fully developed turbulence was present. Furthermore, the grid resolution in most cases was only $4\times$ the fire-polishing length, so it is unclear how much the interaction between turbulence on scales smaller than the fire-polishing length and the flame could have influenced those calculations. Our grid is 512 zones across and almost $30\times$ the fire-polishing length, and as we show, we have a fully developed turbulence on scales between the fire-polishing length and the grid resolution. Finally, we seed more modes, about 10 in each direction compared to 3 in Khokhlov (1994, 1995), which will allow for a longer duration of the non-linear phase of the RT instability.

Provided one does not enter the distributed regime or consider other situations where the physical thickness of the flame itself matters, there should exist a scaling to an arbitrary size domain for regimes having the same reactive Froude number,

$$\mathrm{Fr} = \frac{S_l}{\sqrt{\mathrm{At}\, g L_0}} \sim \sqrt{\frac{\lambda_{\mathrm{fp}}}{L_0}} \tag{14}$$

which evaluates the relative importance of the laminar flame speed to gravity. Our present simulation is at $\mathrm{Fr} = 7 \times 10^{-2}$. Since $(\mathrm{At}\, g)$ is roughly constant throughout the whole explosion, this suggests that our calculation would be very similar to another calculation, e.g., on a length scale of 50 km (1000 times larger than our present one) for a timescale 30 times longer (since $U \sim \sqrt{L}$). Obviously at such a scale, the flame would not be resolved and subgrid structure would be present, but the front geometry for the range of length scales we can model should be the same. A comparison of thickened flames as the same Froude number of the present calculation would be an important validation of that flame model, and is underway. Once validated, our approach offers a path toward bootstrapping to studies that include the entire star. The next step would be to feed turbulence to a flame having the characteristics determined in the present study. That study is also underway.

The results of our three-dimensional resolved study of the reactive RT instability are

encouraging. We have shown that we can accurately model a fully turbulent flame in three dimensions. At late times, as our combustion regimes diagram shows, we just begin to enter the distributed burning regime. There is still a lot of speculation that a transition to detonation can occur in this regime, but our two-dimensional studies (Bell et al. 2004c) suggest that this could not occur. A followup to those studies, well in the distributed regime will be the focus of a later study.

We thank Jens Niemeyer and Alan Kerstein for useful discussions regarding the turbulence and flame interactions, and Frank Timmes for making his equation of state and conductivity routines available online. Support for this work was provided by the DOE grant No. DE-FC02-01ER41176 to the Supernova Science Center/UCSC and the Applied Mathematics Program of the DOE Office of Mathematics, Information, and Computational Sciences under the U.S. Department of Energy under contract No. DE-AC03-76SF00098. SEW acknowledges NASA Theory Award NAG5-12036. The first part of this calculation was performed on the IBM SP (seaborg) at the National Energy Research Scientific Computing Center, which is supported by the Office of Science of the DOE under Contract No. DE-AC03-76SF00098. This calculation was finished on the Columbia system at NASA Ames Research Center. We are grateful to both centers for the computer time. Movies of the simulations are available at http://www.ucolick.org/~zingale/rt3d/.

REFERENCES

Bell, J. B., Day, M. S., Rendleman, C. A., Woosley, S. E., & Zingale, M. A. 2004a, Journal of Computational Physics, 195, 677

—. 2004b, Astrophysical Journal, 606, 1029

—. 2004c, Astrophysical Journal, 608, 883

Berger, M. J., & Colella, P. 1989, J. Comp. Phys., 82, 64

Calder, A. C., Fryxell, B., Plewa, T., Rosner, R., Dursi, L. J., Weirs, V. G., Dupont, T., Robey, H. F., Kane, J. O., Remington, B. A., Drake, R. P., Dimonte, G., Zingale, M., Timmes, F. X., Olson, K., Ricker, P., MacNeice, P., & Tufo, H. M. 2002, ApJS, 143, 201

Caughlan, G. R., & Fowler, W. A. 1988, Atomic Data and Nuclear Data Tables, 40, 283, see also http://www.phy.ornl.gov/astrophysics/data/cf88/index.html

Chertkov, M. 2003, Phys. Rev. Letters, 91, 115001

Colin, O., Ducros, F., Veynante, D., & Poinsot, T. 2000, Phys. of Fluids, 12, 1843

Davies, R. M., & Taylor, G. 1950, Proc. R. Soc. London A, 200, 375

Dimonte, G., Youngs, D. L., Dimits, A., Weber, S., Marinak, M., Wunsch, S., Garasi, C., Robinson, A., Andrews, M. J., Ramaprabhu, P., Calder, A. C., Fryxell, B., Biello, J., Dursi, L., MacNeice, P., Olson, K., Ricker, P., Rosner, R., Timmes, F., Tufo, H., Young, Y.-N., & Zingale, M. 2004, Phys. of Fluids, 16, 1668

Dursi, L. J., Zingale, M., Calder, A. C., Fryxell, B., Timmes, F. X., Vladimirova, N., Rosner, R., Caceres, A., Lamb, D. Q., Olson, K., Ricker, P. M., Riley, K., Siegel, A., & Truran, J. W. 2003, ApJ, 595, 955

Gamezo, V. N., Khokhlov, A. M., Oran, E. S., Chtchelkanova, A. Y., & Rosenberg, R. O. 2003, Science, 299, 77

Khokhlov, A. 1993, ApJ, 419, L77+

—. 1994, ApJ, 424, L115

Khokhlov, A. M. 1995, ApJ, 449, 695

Livne, E. 1993, ApJ, 406, L17

Müller, E., & Arnett, W. D. 1982, ApJ, 261, L109

Niemeyer, J. C., Bushe, W. K., & Ruetsch, G. R. 1999, ApJ, 524, 290

Niemeyer, J. C., & Hillebrandt, W. 1995, ApJ, 452, 769

Niemeyer, J. C., & Kerstein, A. R. 1997, New Astronomy, 2, 239

Niemeyer, J. C., & Woosley, S. E. 1997, ApJ, 475, 740

Peters, N. 2000, Turbulent Combustion (Cambridge University Press)

Poinsot, T., & Veynante, D. 2001, Theoretical and Numerical Combustion (R. T. Edwards)

Röpke, F. K., & Hillebrandt, W. 2005, A&A, 429, L29

Reinecke, M., Hillebrandt, W., & Niemeyer, J. C. 2002, A&A, 391, 1167

Rendleman, C. A., Beckner, V. E., Lijewski, M., Crutchfield, W. Y., & Bell, J. B. 2000, Computing and Visualization in Science, 3, 147

Röpke, F. K., Niemeyer, J. C., & Hillebrandt, W. 2003, ApJ, 588, 952

Sharp, D. H. 1984, Physica, 12D, 3

Timmes, F. X. 2000, ApJ, 528, 913

Timmes, F. X., & Swesty, F. D. 2000, ApJS, 126, 501

Timmes, F. X., & Woosley, S. E. 1992, ApJ, 396, 649

Young, Y.-N., Tufo, H. M., Dubey, A., & Rosner, R. 2001, J. Fluid Mech., 447, 377

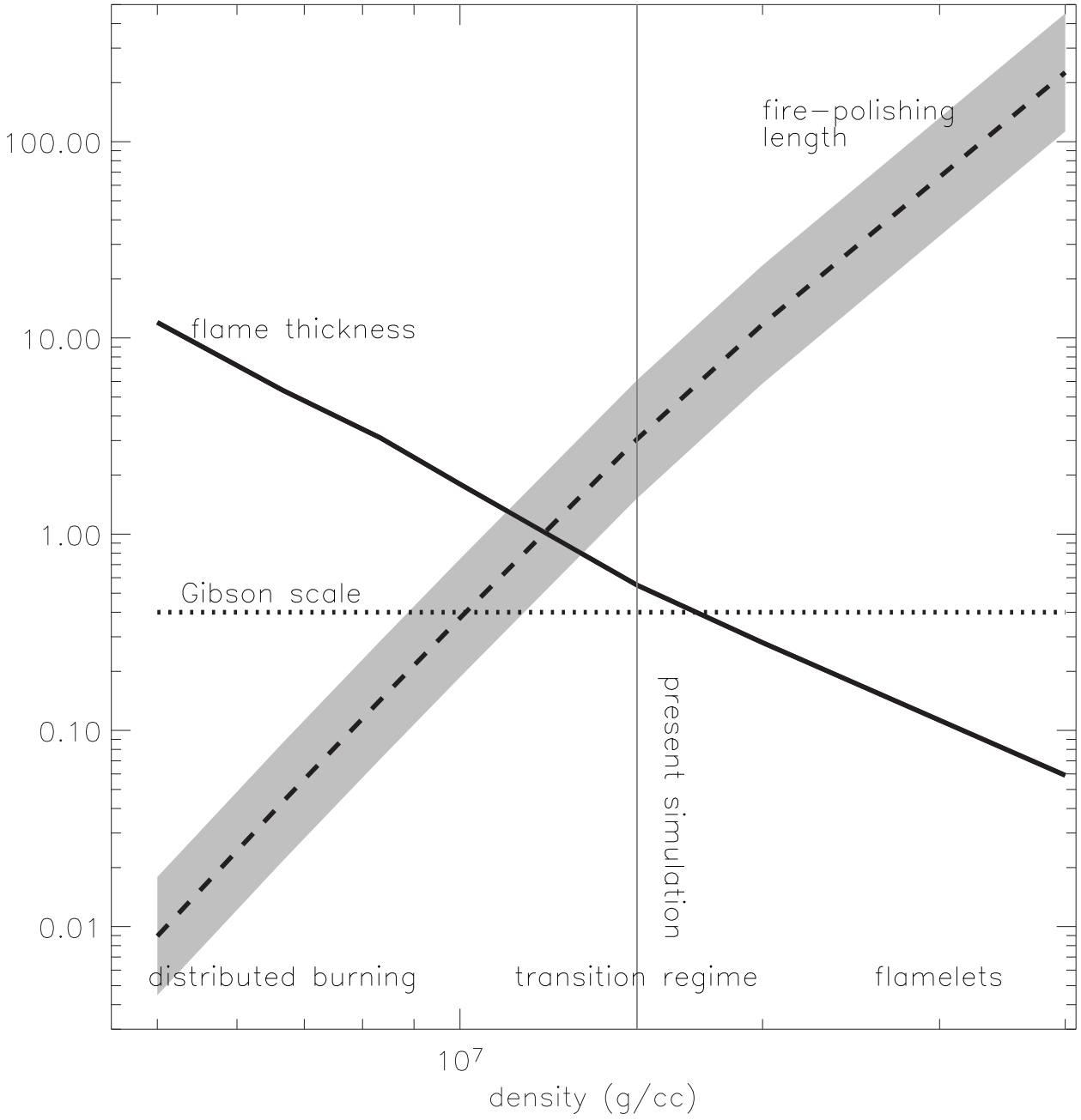

Fig. 1.— Flame thickness (solid), fire-polishing length (dashed), and Gibson scale (dotted) as a function of density. The shaded region reflects a factor of two uncertainty in the fire-polishing length, due either to changing gravitation acceleration or uncertainty in the multiplicative constant. We see the fire-polishing length and flame thickness lines crossing at a density between 10^7 g cm^{-3} and 1.5×10^7 g cm^{-3}. The Gibson scale line is at the measured value for the present three-dimensional simulation (see § 3). At the high density side, we are in the flamelet regime. At low densities, we are in the distributed burning regime.

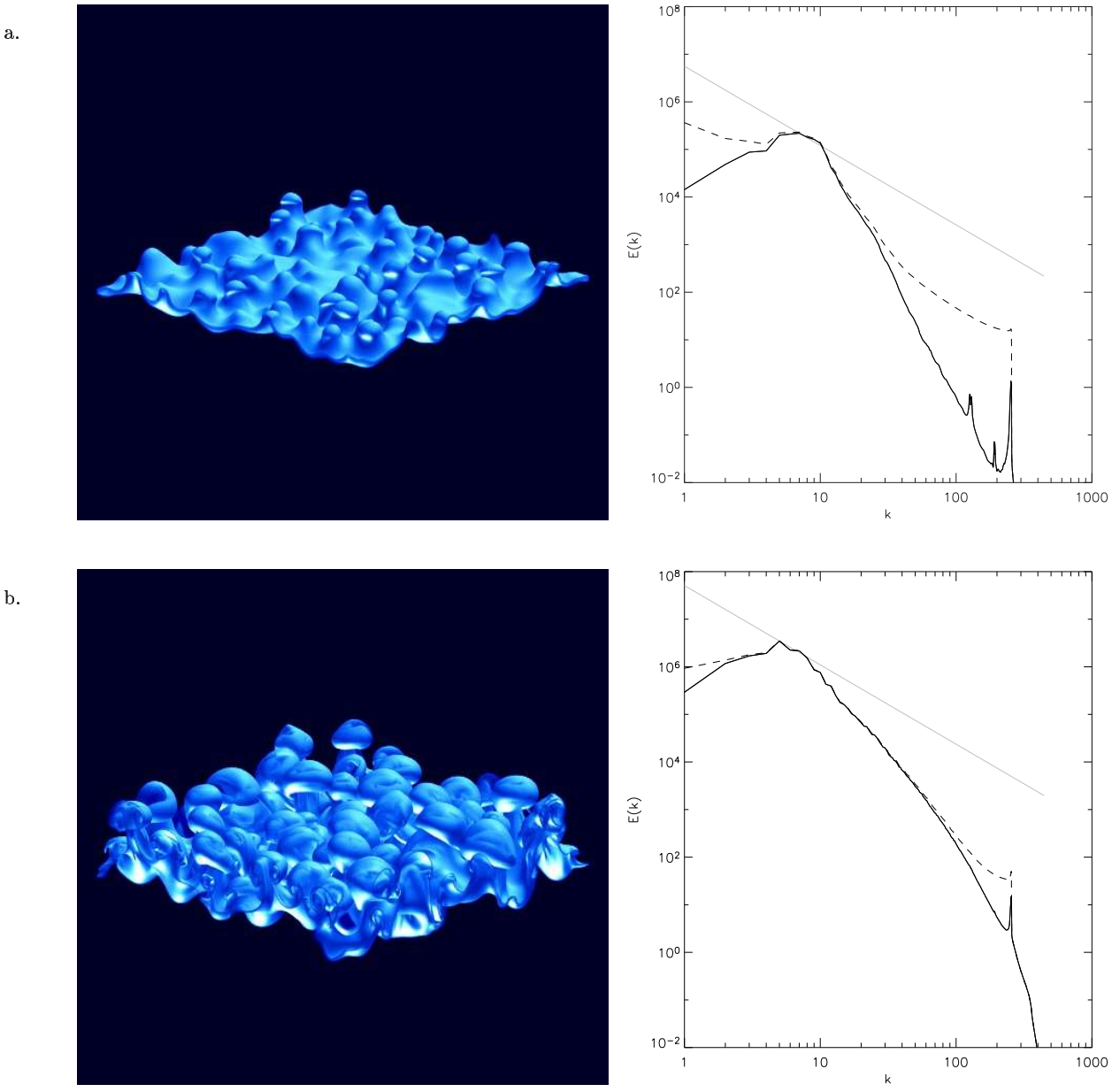

Fig. 2.— Volume rendering of the carbon mass fraction (left) and the kinetic energy power spectrum (right) at (a) 4.04×10^{-4} s, (b) 6.62×10^{-4} s, (c) 8.11×10^{-4} s, (d) 9.43×10^{-4} s, (e) 1.07×10^{-3} s, and (f) 1.16×10^{-3} s. The dark solid curve is the power spectrum after projecting out the compressible components. The dashed curve is without the projection. The gray line is a $-5/3$ power law. We see that at late times, we reach a Kolmogorov scaling.

c.

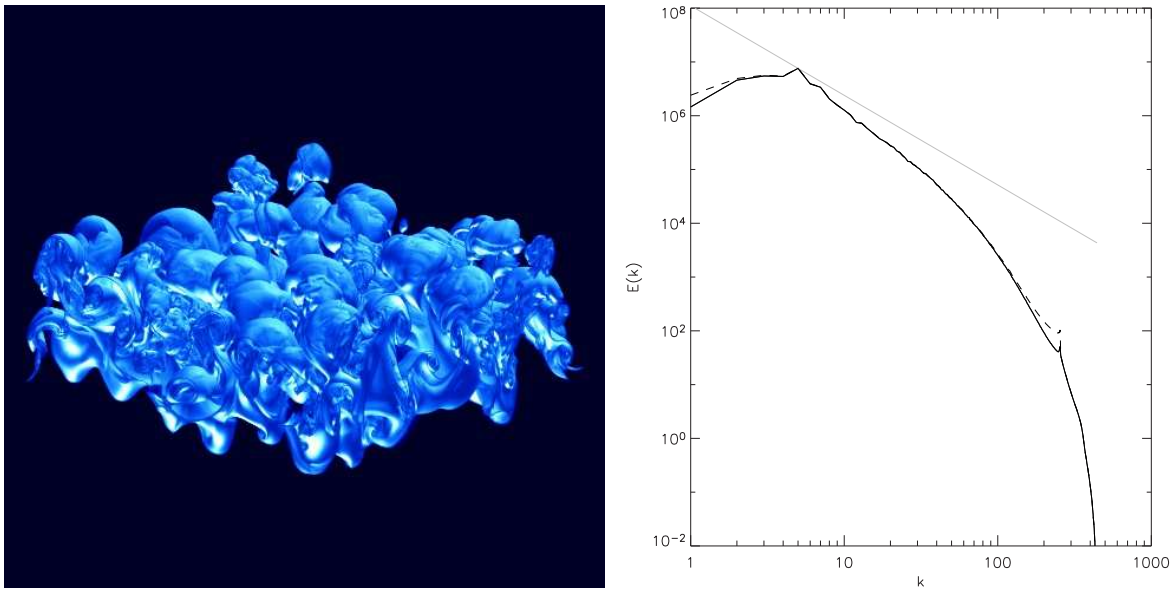
10^8
10^6
10^4
10^2
10^0
10^{-2}
E(k)
1
10
100
1000
k

d.

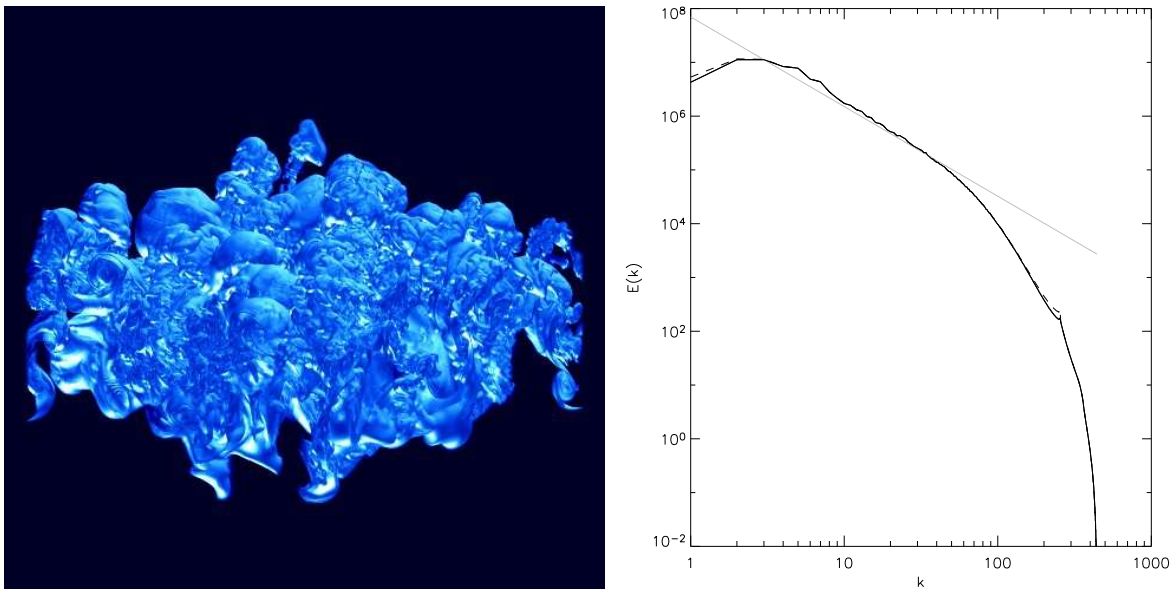
10^8
10^6
10^4
10^2
10^0
10^{-2}
E(k)
1
10
100
1000
k

Fig. 2.— cont.

e.

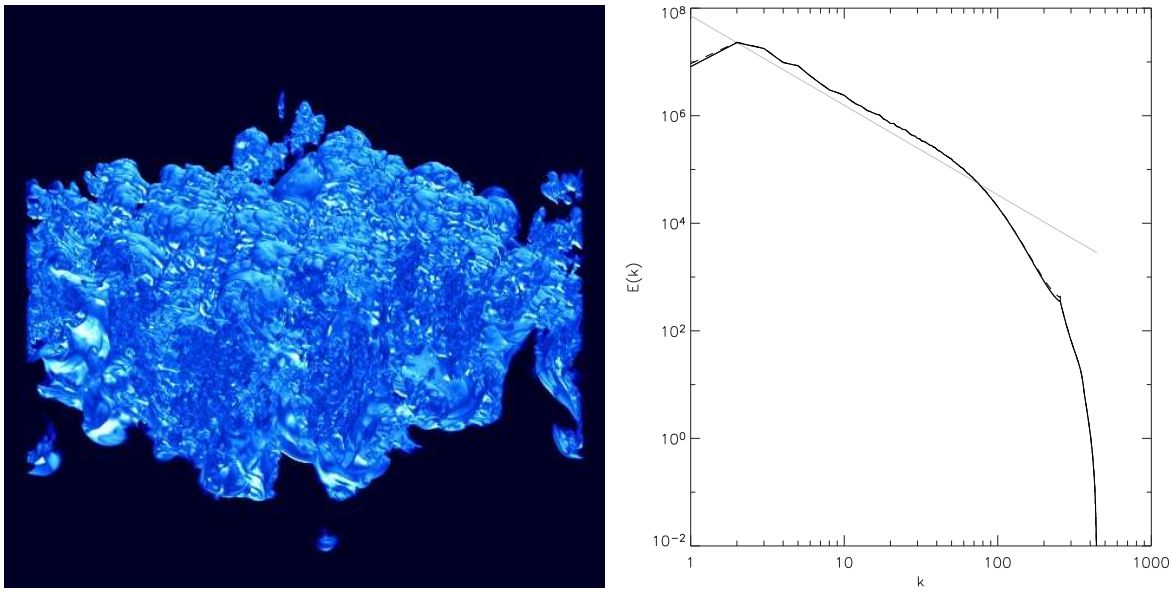
10^8
10^6
10^4
10^2
10^0
10^{-2}
E(k)
1
10
100
1000
k

f.

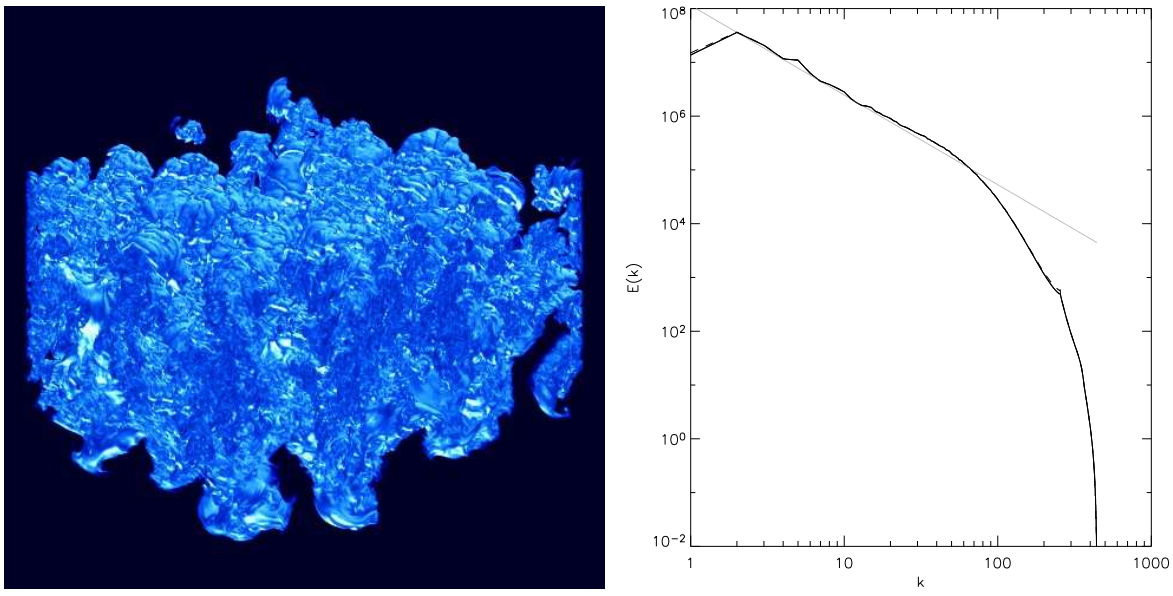
10^8
10^6
10^4
10^2
10^0
10^{-2}
E(k)
1
10
100
1000
k

Fig. 2.— cont.

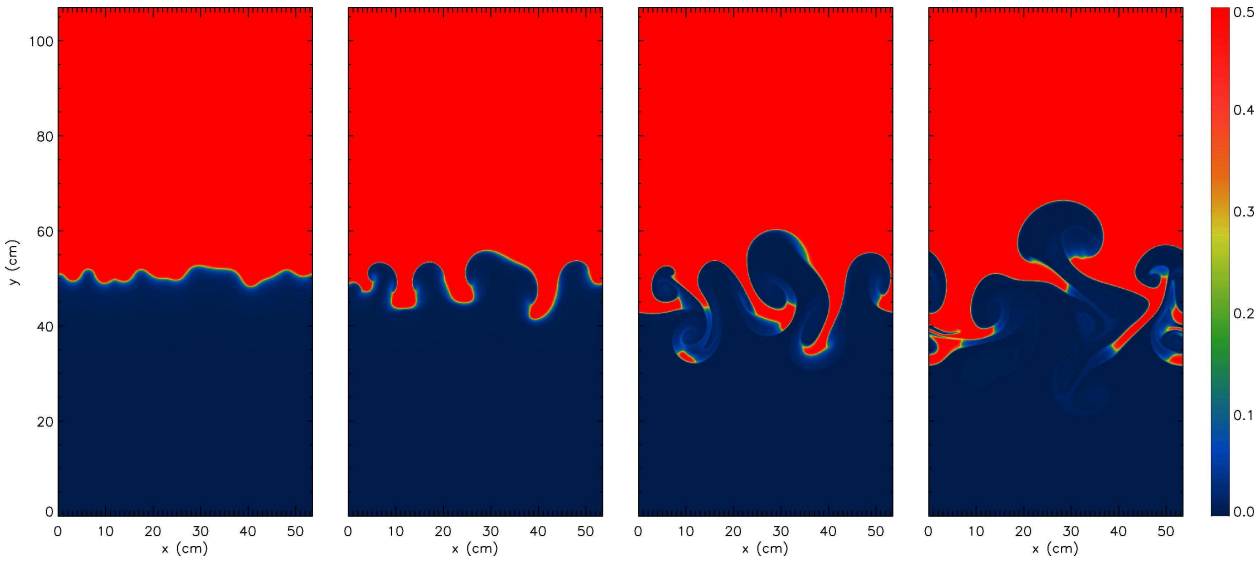

Fig. 3.— Carbon mass fraction for the two-dimensional simulation at 2.5×10^{-4}, 5×10^{-4}, 7.5×10^{-4}, and 10^{-3} s. In two dimensions, the turbulence does not reach the small scales, resulting in a much smoother flame.

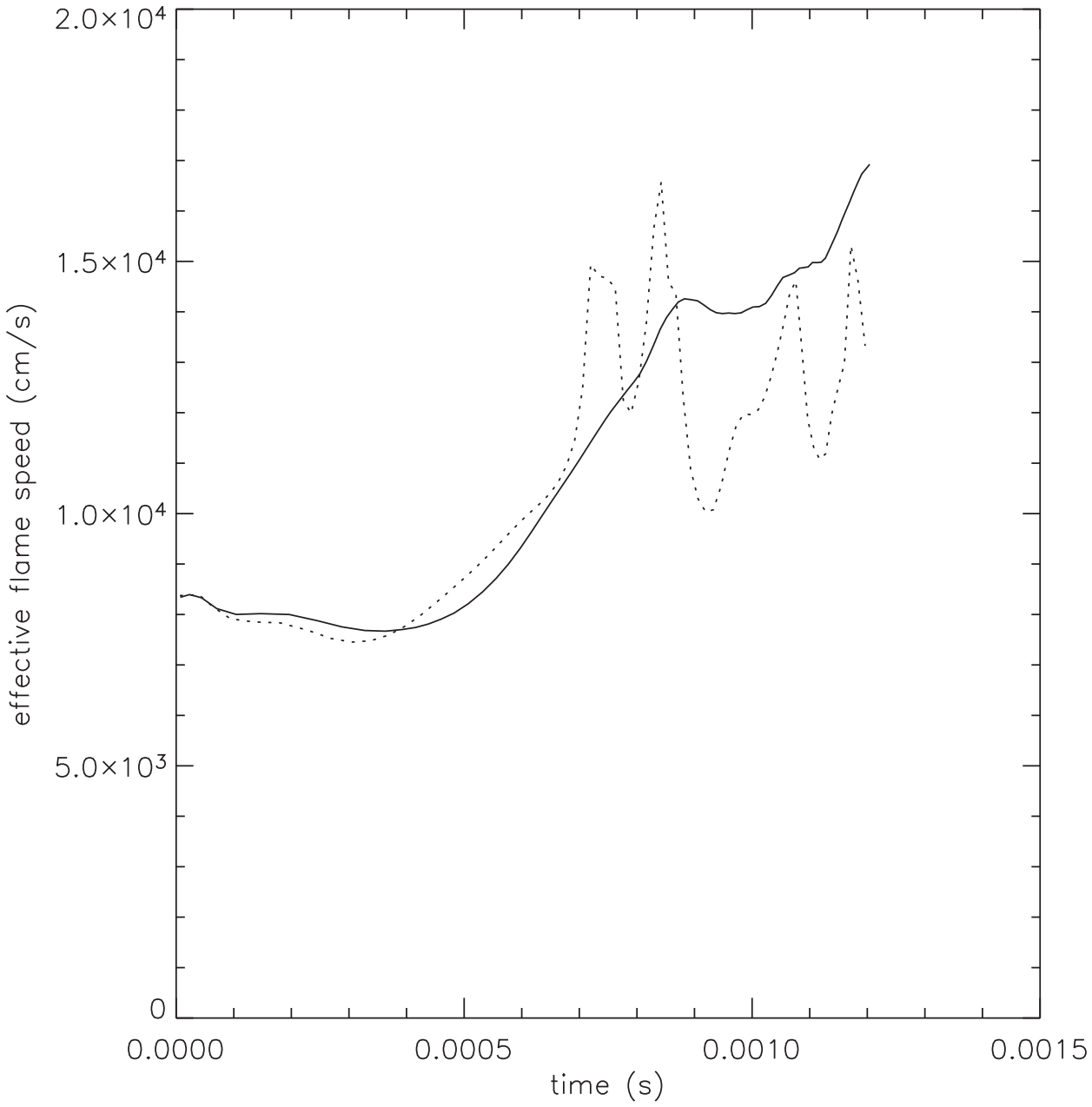

Fig. 4.— Effective flame speed for the 2d (dotted) and 3d (solid) flame simulations. The acceleration at late times in the 3d simulation is due to the onset of turbulence.

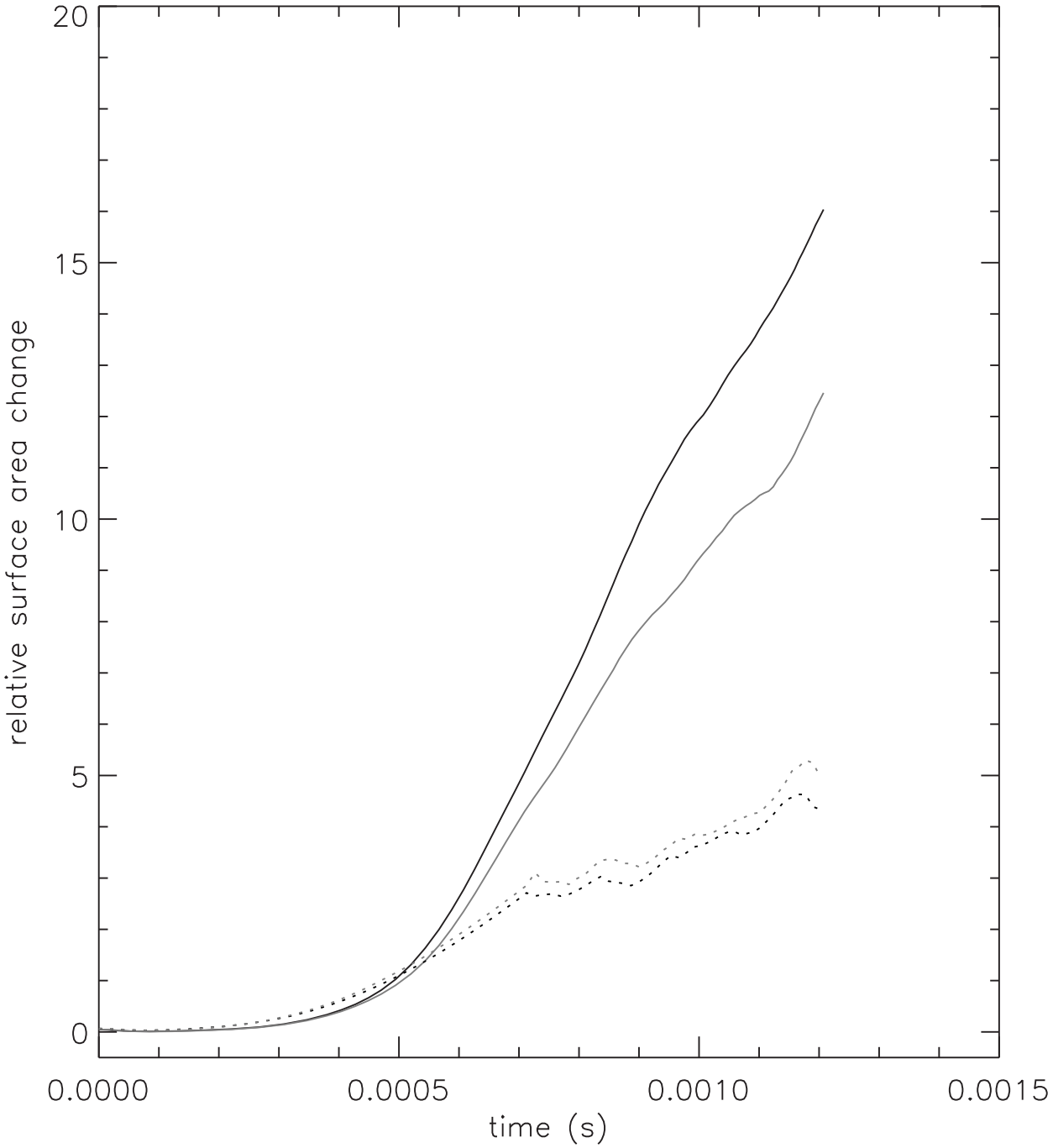

Fig. 5.— Relative surface area change for the two-dimensional (dotted) and three-dimensional (solid) flame simulations. Two curves are shown for each dimensionality, corresponding to a carbon mass fraction of 0.25 (black) and 0.1 (gray). In three dimensions, the relative change in surface area is far larger than the two-dimensional case, but the flame speed changes are about the same (Figure 4), demonstrating the larger effect of curvature and strain on the local burning rate.

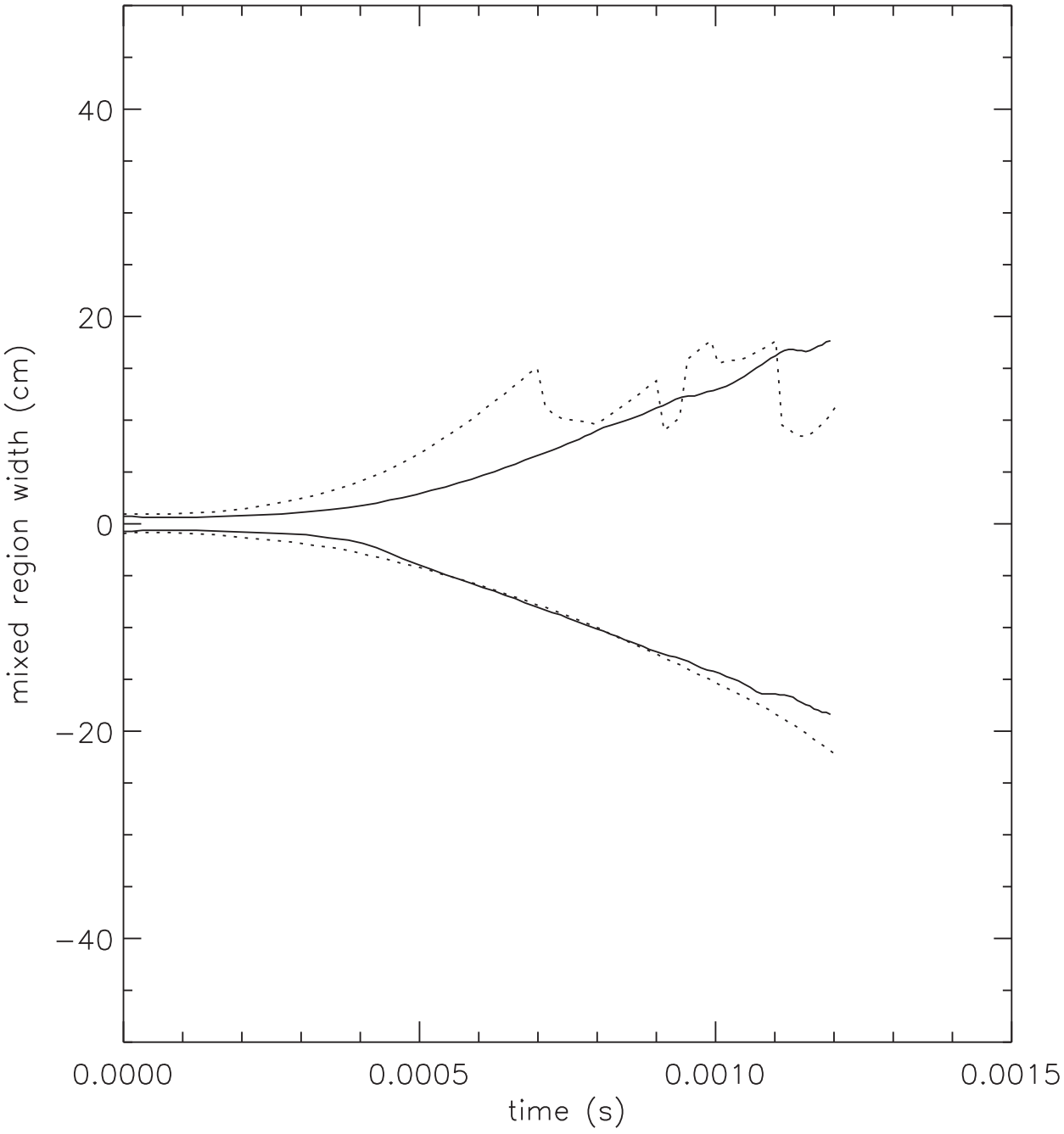

Fig. 6.— Extent of the mixed region for the 2d (dotted) and 3d (solid) flame simulations. We see that the position of the spikes of fuel moving into the hot ash (top curves) is greatly suppressed in three dimensions, owing to the greater surface to volume area enhancing the burning.

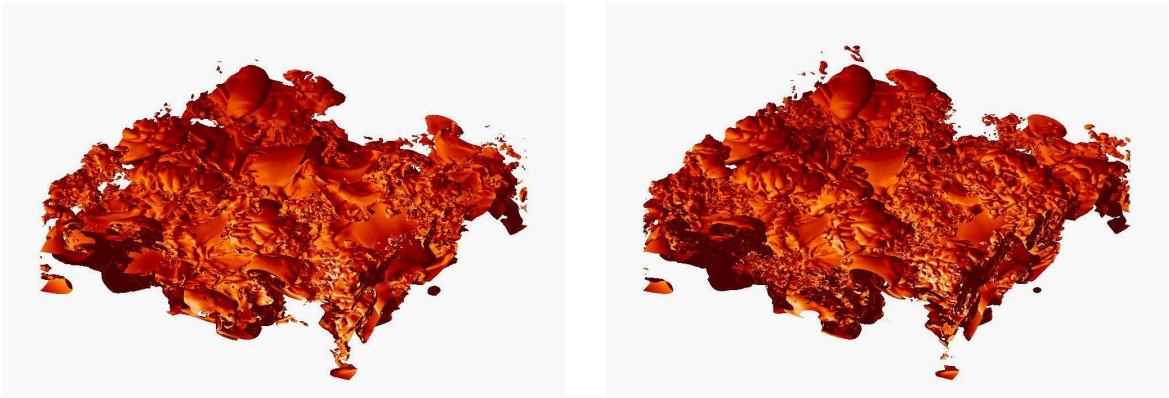

Fig. 7.— Isosurfaces of the carbon mass fraction of 0.1 (left) and 0.25 (right) at 10^{-3} s.

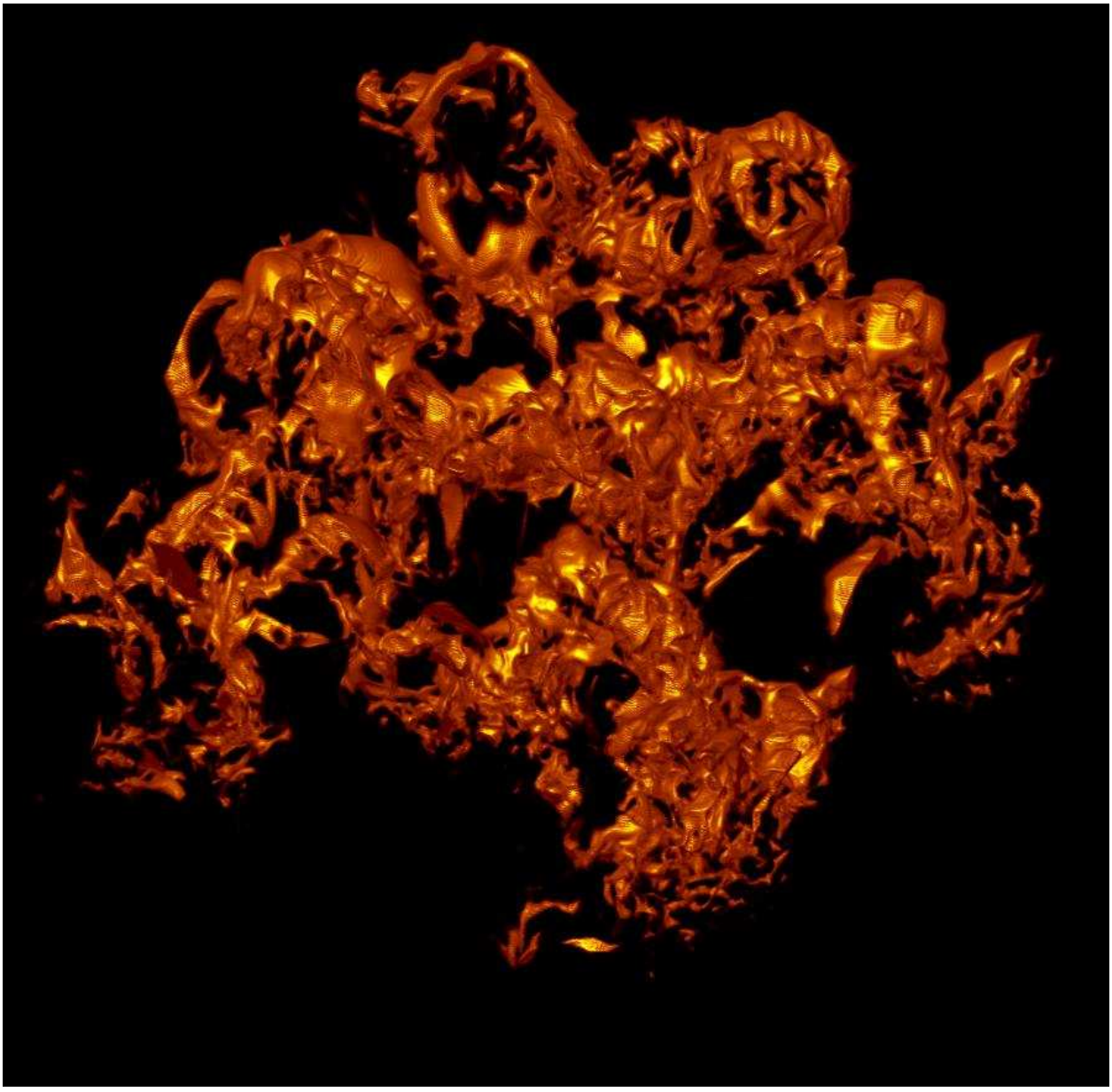

Fig. 8.— Volume rendering of the carbon destruction rate at 1.16×10^{-3} s, showing the reacting surface is not uniform.

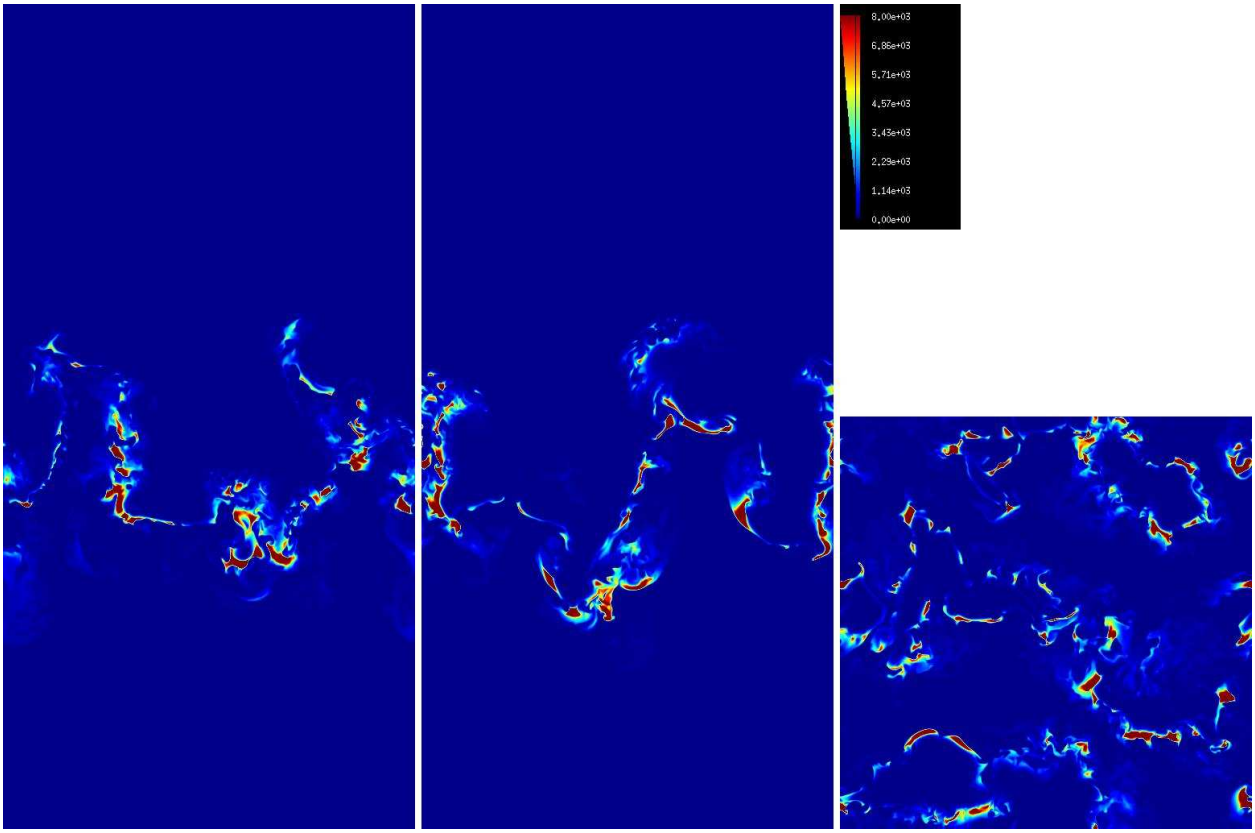

Fig. 9.— Slices of the absolute value of the carbon destruction rate at 1.16×10^{-3} s, for the three-dimensional calculation. Shown at $x-z$ (left), $y-z$ (center), and $x-y$ (right). These provide an alternate view to the volume rendering in Figure 8. In this plot, the limits of the colormap are chosen to match the laminar burning rates.

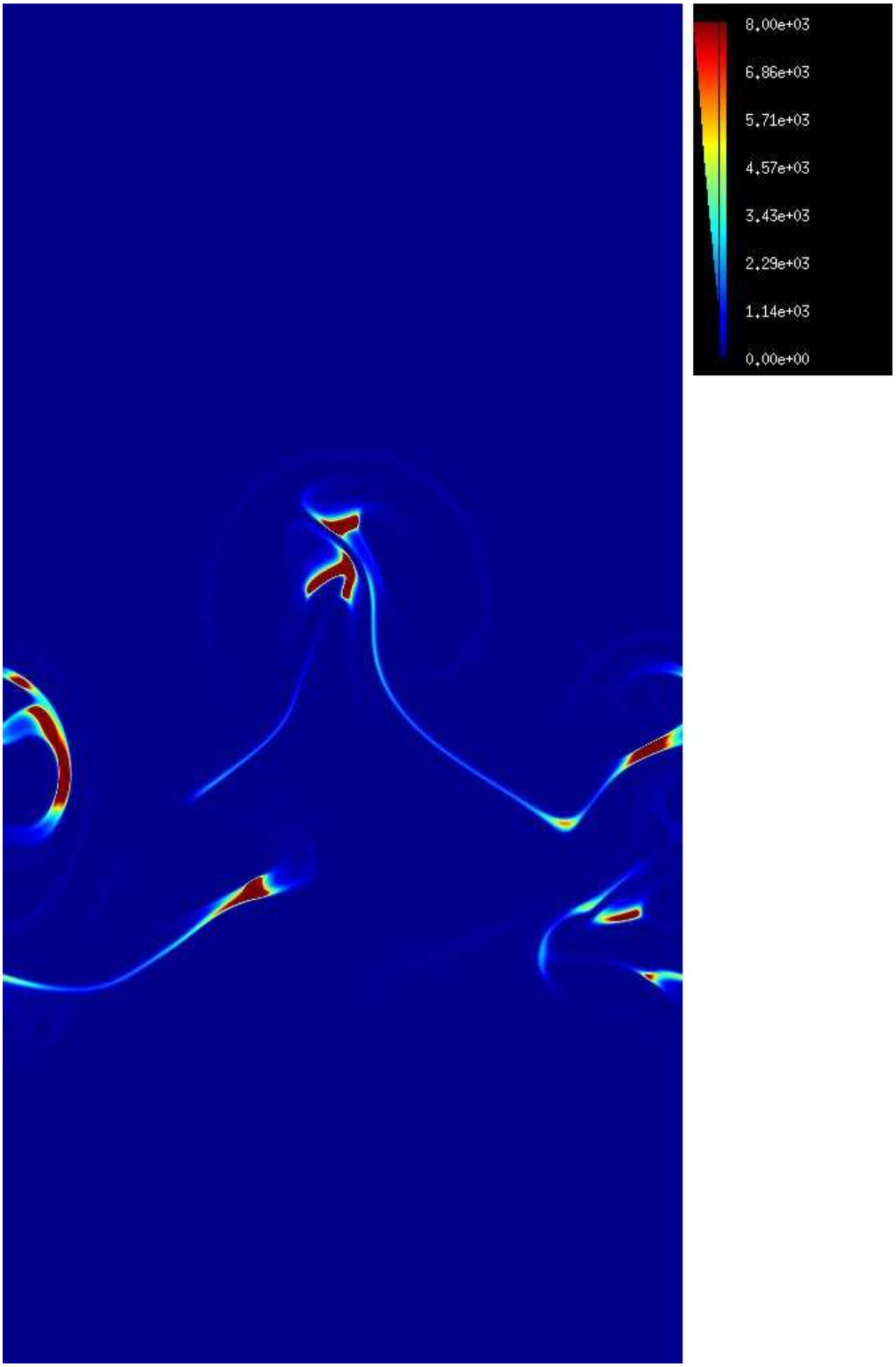

Fig. 10.— Absolute value of the carbon destruction rate for the two-dimensional calculation at $1.16 \times 1-^{-3}$ s. The limits of the colormap are chosen to match the laminar burning rates, so regions that are deep red are burning faster than laminar.

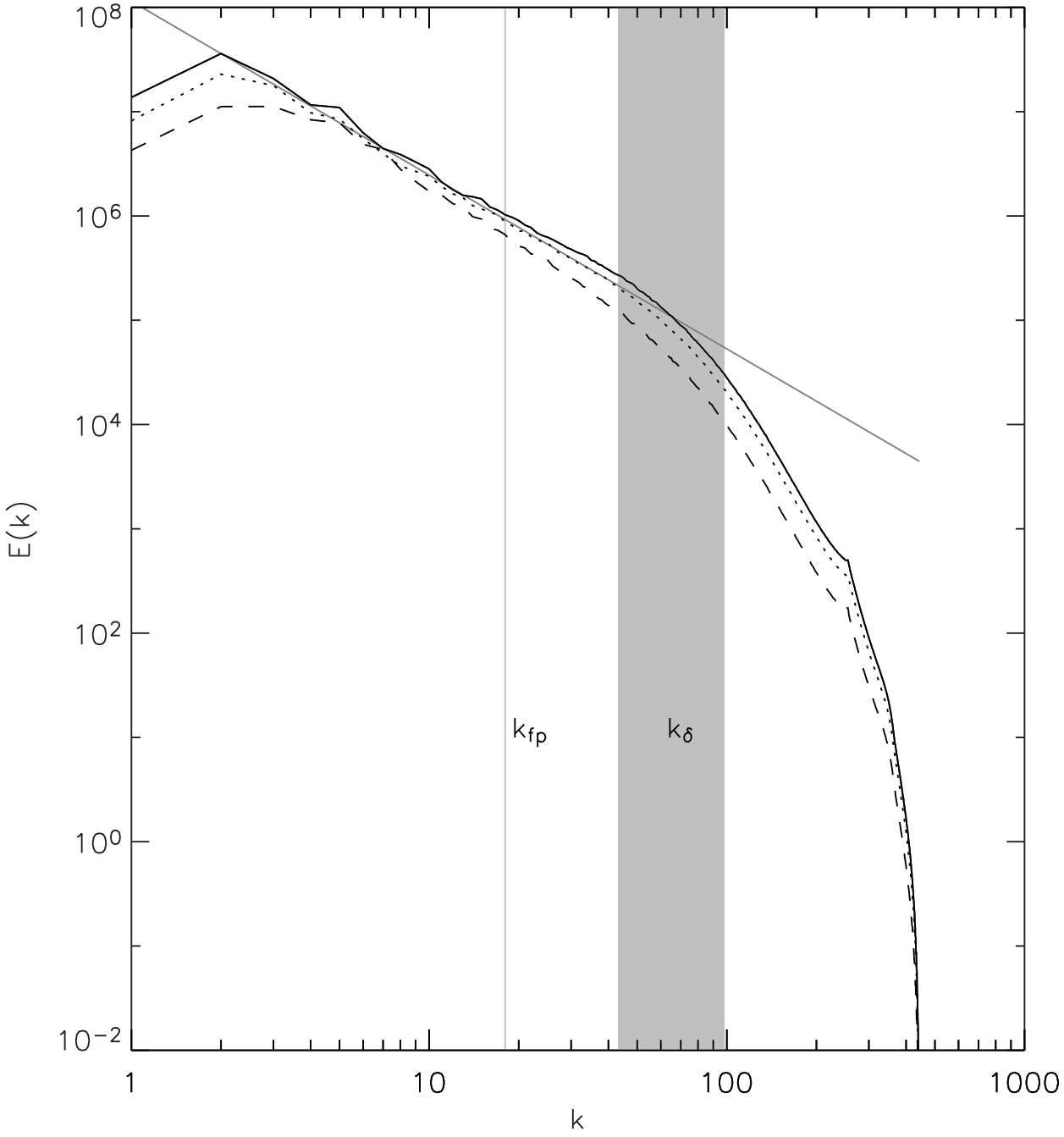

Fig. 11.— Late time turbulence power spectra corresponding to panel d (black solid line), e (dotted line), and f (dashed line) of Figure 2. The straight gray line is a $-5/3$ power law. Here we see that the small scale cutoff to the Kolmogorov spectrum does not shift with time with this fully developed turbulence. The position of the fire-polishing wavenumber, $k_{\rm fp}$ and the range of flame thickness spanned by our two definitions, k_δ, are shown as well.

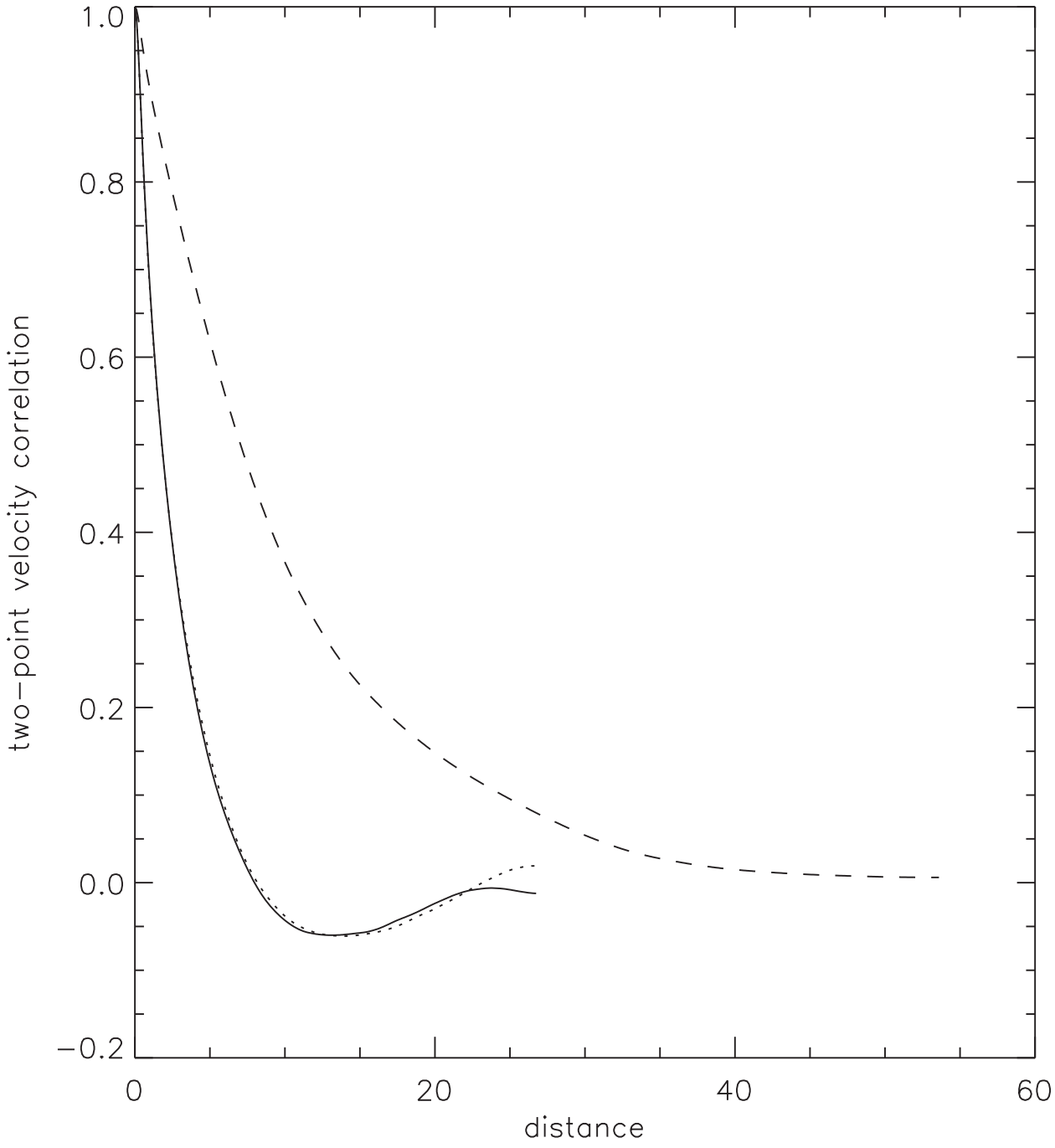

Fig. 12.— Two-point correlation for data in Figure 2f in each coordinate direction: x (solid), y (dotted), and z (dashed). We see that in the z-direction, the correlation length scale is much higher than in the transverse directions. In the transverse directions, the data is anti-correlated between 8 and 23 cm.

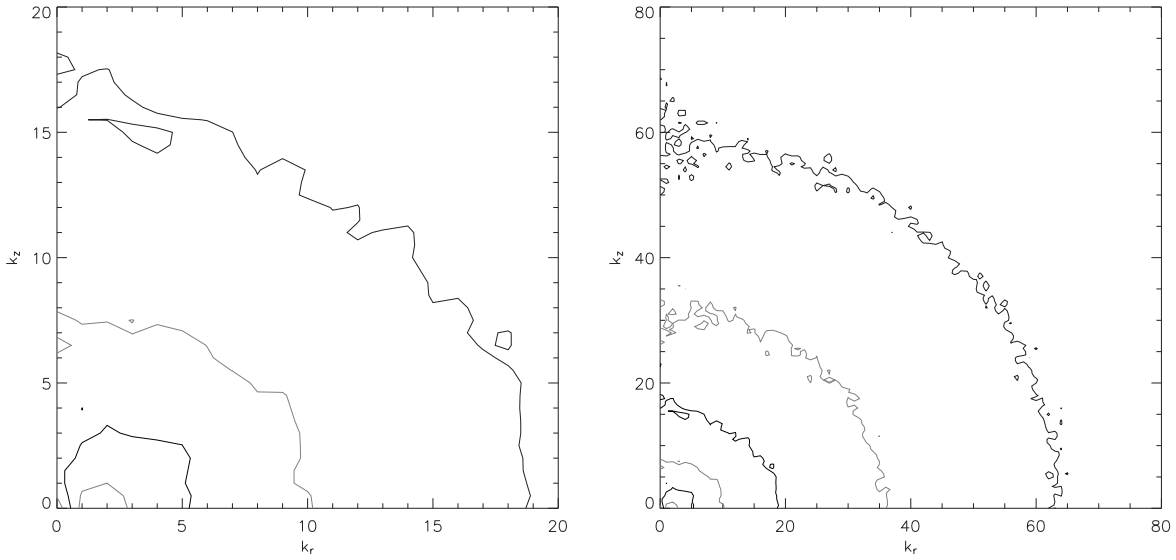

Fig. 13.— Contours of the cylindrically averaged Fourier transform of the turbulent kinetic energy, $E(k_r, k_z)$ shown at $E = 10^6$, 10^5, 10^4, 10^3, 10^2, and 10 cm^2 s^{-2}, moving outward from the origin. The left panel shows a close up of the origin. Small wave numbers correspond to large length scales, and we see that at the very smallest wavenumbers, we are significantly anisotropic, but as the cascade moves to larger wavenumbers, we become more and more isotropic.

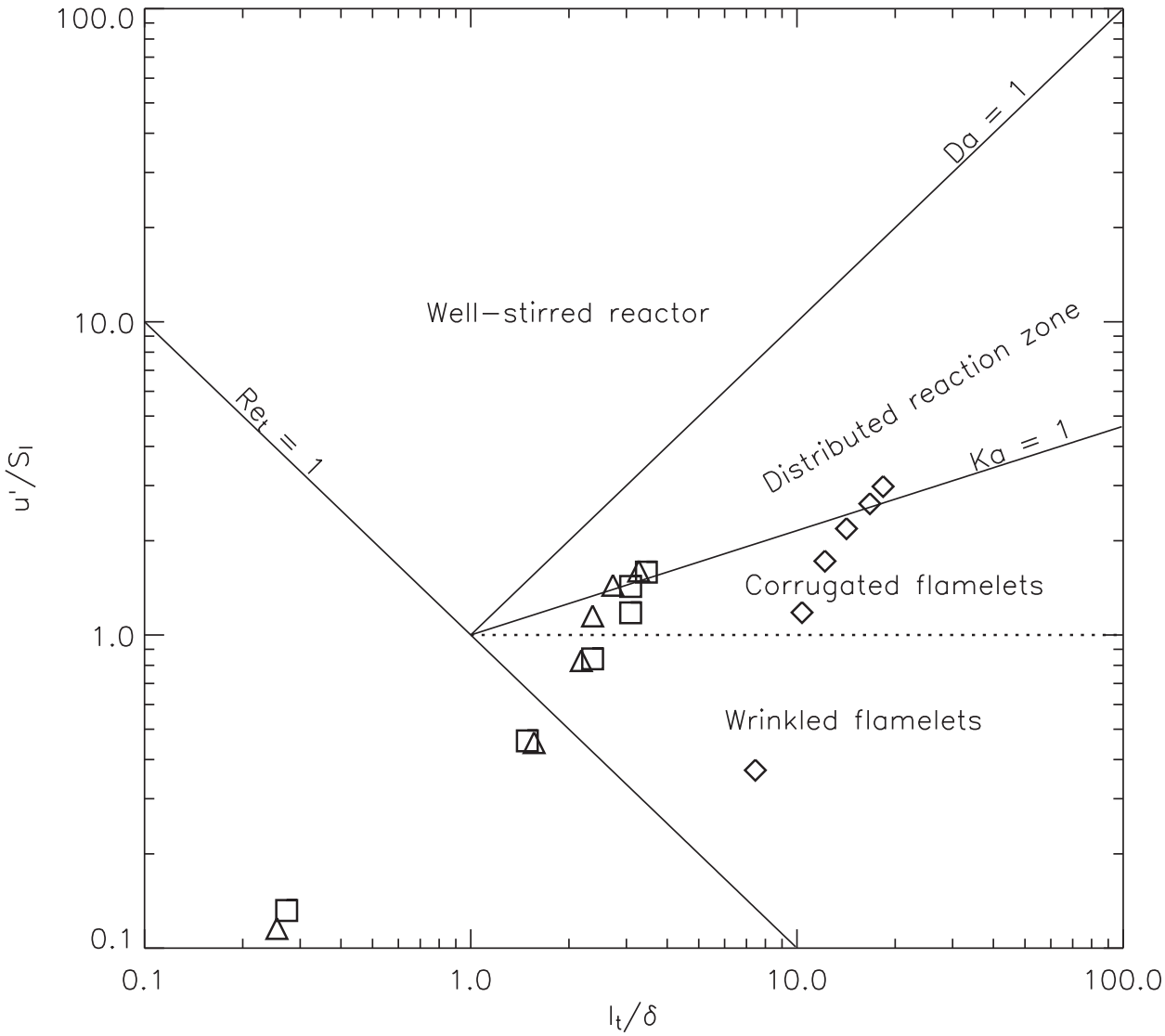

Fig. 14.— Combustion regimes diagram (Poinsot & Veynante 2001) using the turbulent intensity and integral scale for the six timesteps shown in Figure 2. Because our turbulence is so anisotropic, we plot each timestep three times, once using the x data (triangles), the y data (squares), and the z data. In all cases, the flame moves to the top-right as it evolves, just passing into the distributed regime at the end of the calculation.

Table 1: Integral length scale and turbulent intensities.

key[a]	time (s)	$l_t^{(x)}$ (cm)	$l_t^{(y)}$ (cm)	$l_t^{(z)}$ (cm)	u' (cm s^{-1})	v' (cm s^{-1})	w' (cm s^{-1})
a	4.04×10^{-4}	0.14	0.15	4.1	9.48×10^{2}	1.08×10^{3}	3.03×10^{3}
b	6.62×10^{-4}	0.86	0.82	5.7	3.71×10^{3}	3.76×10^{3}	9.66×10^{3}
c	8.11×10^{-4}	1.2	1.3	6.7	6.78×10^{3}	6.87×10^{3}	1.41×10^{4}
d	9.43×10^{-4}	1.3	1.7	7.8	9.42×10^{3}	9.64×10^{3}	1.79×10^{4}
e	1.07×10^{-3}	1.5	1.7	9.2	1.18×10^{4}	1.17×10^{4}	2.15×10^{4}
f	1.16×10^{-3}	1.8	1.9	10.1	1.31×10^{4}	1.30×10^{4}	2.44×10^{4}

[a]see Figure 2.